

## Direct measurement and modeling of the redirected ion flux in a high-powered pulsed-plasma magnetron

Liang Meng, He Yu, John R. Sporre, Priya Raman, Matthew M. Szott, Jake T. McLain, and David N. Ruzic

Citation: *Journal of Vacuum Science & Technology A* **33**, 031301 (2015); doi: 10.1116/1.4914174

View online: <http://dx.doi.org/10.1116/1.4914174>

View Table of Contents: <http://scitation.aip.org/content/avs/journal/jvsta/33/3?ver=pdfcov>

Published by the AVS: Science & Technology of Materials, Interfaces, and Processing

### Articles you may be interested in

[Downstream plasma transport and metal ionization in a high-powered pulsed-plasma magnetron](#)

*J. Appl. Phys.* **115**, 223301 (2014); 10.1063/1.4878622

[Study on the effect of target on plasma parameters of magnetron sputtering discharge plasma](#)

*Phys. Plasmas* **20**, 103505 (2013); 10.1063/1.4825235

[Drifting localization of ionization runaway: Unraveling the nature of anomalous transport in high power impulse magnetron sputtering](#)



*J. Appl. Phys.* **111**, 053304 (2012); 10.1063/1.3692978

[Dynamics of reactive high-power impulse magnetron sputtering discharge studied by time- and space-resolved optical emission spectroscopy and fast imaging](#)

*J. Appl. Phys.* **107**, 043305 (2010); 10.1063/1.3305319

[Influence of pulse duration on the plasma characteristics in high-power pulsed magnetron discharges](#)

*J. Appl. Phys.* **99**, 013307 (2006); 10.1063/1.2159555

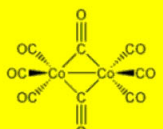
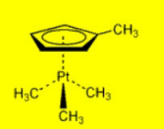
Corporate Headquarters  
Newburyport, MA USA

European Office  
Bischheim, France

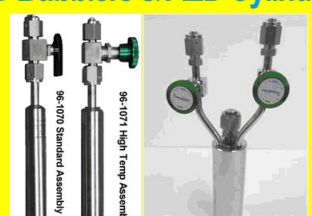
[Visit strem.com/cvd](http://strem.com/cvd)

### Over 350 CVD & ALD Precursors

- metal alkyls
- metal alkoxides
- metal  $\beta$ -diketonates
- volatile organometallics
- electronic grade chemicals

### CVD Bubblers & ALD Cylinders



DOT and UN approved configurations available as well as precursor filling & refilling services.

# Direct measurement and modeling of the redirected ion flux in a high-powered pulsed-plasma magnetron

Liang Meng<sup>a)</sup>

*Department of Nuclear Plasma and Radiological Engineering, Center for Plasma Material Interactions, University of Illinois at Urbana-Champaign, Urbana, Illinois 61801*

He Yu

*Department of Nuclear Plasma and Radiological Engineering, Center for Plasma Material Interactions, University of Illinois at Urbana-Champaign, Urbana, Illinois 61801 and State Key Laboratory of Electronic Thin Films and Integrated Devices, School of Optoelectronic Information, University of Electronic Science and Technology of China, Chengdu 610054, People's Republic of China*

John R. Sporre, Priya Raman, Matthew M. Szott, Jake T. McLain, and David N. Ruzic

*Department of Nuclear Plasma and Radiological Engineering, Center for Plasma Material Interactions, University of Illinois at Urbana-Champaign, Urbana, Illinois 61801*

(Received 29 November 2014; accepted 23 February 2015; published 16 March 2015)

Self-sputtering is a crucial feature in high-powered pulsed magnetron sputtering (HPPMS). A direct measurement of the recirculating ion fluxes to the target, however, has not been made until now using a specially designed magnetron system. A small orifice was drilled in the target, allowing plasma fluxes to penetrate and be diagnosed subsequently. Ion currents of the penetrating copper ions ( $\text{Cu}^+$ ) and argon ions ( $\text{Ar}^+$ ) were collected on biased grids, while Cu depositions were measured on witness Si wafers. Based on these measurements, fluxes of  $\text{Cu}^+$  ions and  $\text{Ar}^+$  ions were differentiated. For a tested condition, the ratio of  $\text{Cu}^+$  density to  $\text{Ar}^+$  density was determined to be  $1.5 \pm 0.3$ , indicating a strong self-sputtering effect during HPPMS. Using a semiempirical plasma model, this ratio was predicted to be 1.4 within plasma, matching well with the measurement. The model calculates the evolution of various plasma species in the strong ionization region and thus allows a quick estimation of some key HPPMS parameters such as  $\text{Cu}^+$  ionization fraction and  $\text{Cu}^+$  to  $\text{Ar}^+$  density ratio in a time-resolved manner. The ion currents were observed to increase abruptly after a certain time delay, longer for a lower pulse voltage. This suggests a mechanism that the plasma is only ignited initially in a stripe along the sputtering “racetrack” where the magnetic field ( $B$ ) is strong enough. At a higher pulse voltage, the ignition plasma stripe became longer and drifted faster parallel to the target toward the region of weak magnetic field. © 2015 American Vacuum Society. [<http://dx.doi.org/10.1116/1.4914174>]

## I. INTRODUCTION

Magnetron sputtering is a commonly used technique for physical vapor deposition (PVD). It enhances the plasma in vicinity of the target by magnetically confining the electrons. For many applications, it is beneficial to further increase the ion fluxes of the sputtered materials, as the so-called ionized PVD (iPVD).<sup>1,2</sup> One of the methods to achieve iPVD is to apply a very high pulsed voltage to the magnetron to generate dense plasmas and promote the ionization process.<sup>3,4</sup> This technique was developed in the 1990s and is commonly known as high-power pulsed magnetron sputtering (HPPMS). When high pulse voltage (around 1 kV) is applied to the target, peak power density of  $\text{kW}/\text{cm}^2$  can be produced. Dense plasmas of  $10^{19}$ – $10^{20} \text{ m}^{-3}$  are generated in front of the target. This is generally referred to as high-powered impulse magnetron sputtering (HiPIMS).<sup>5</sup> There are other variations of HPPMS technique, including the modulated pulse power technique.<sup>6,7</sup> In current study, HPPMS is used because of slightly lower power density than the typical value of  $>500 \text{ W}/\text{cm}^2$  in HiPIMS. HPPMS has

been applied to a wide range of processes, showing great benefits in improving film qualities, modifying film properties, and allowing processing in small recessed structures.<sup>8–11</sup> The highly ionized sputtered materials are believed to be critical for these benefits.

Extensive studies have been performed to understand the mechanisms involved with the high ionization in HiPIMS. Various types of plasma diagnostics have been used to characterize the temporal evolution and transport of the HiPIMS plasma.<sup>12–17</sup> The intense plasmas greatly promote the ionization of the sputtered materials, as observed using optical emission spectroscopy, absorption spectroscopy, mass spectroscopy, and gridded energy analyzer combined with quartz crystal microbalance (QCM).<sup>17–20</sup> Strong rarefaction effect<sup>21</sup> has been observed, e.g., gas atoms being depleted in the target vicinity by the high flux of sputtered materials.<sup>22,23</sup> The increased metal ionization in HiPIMS leads to enhanced self-sputtering, i.e., the target being sputtered by the metal ions. A sustained self-sputtering can be achieved for certain target materials with high enough pulse voltage and current.<sup>24</sup> Self-sputtering, in conjunction with gas recycling,<sup>25</sup> leads to the runaway to the high density discharge. Strong localization of ionization, instead of uniform plasma over a

<sup>a)</sup>Electronic mail: lmeng3@gmail.com

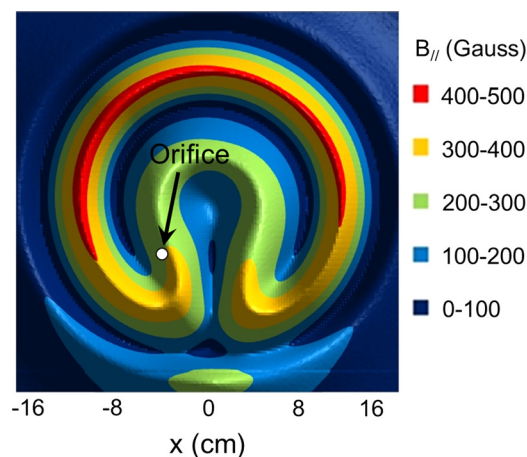


FIG. 1. (Color online) Location of the orifice as shown in the  $B_{\parallel}$  mapping on the target surface.

magnetron's erosion racetrack, has also been discovered as a unique mechanism during HiPIMS.<sup>26-29</sup>

These unique mechanisms are seldom studied by directly measuring the recirculating ion fluxes, with concerns of strongly disturbing the plasma near the target. Indirect methods such as optical spectroscopy and fast camera are commonly used instead. These methods are typically hard to quantify or lack good spatial resolution. In the present study, a new method to sample the plasma fluxes through an orifice in the racetrack region is implemented. The penetrating ion currents are collected on biased grids while the metal deposition flux is measured using witness Si wafers. The metal ions and gas ions can then be differentiated.

HiPIMS plasma modeling has been developed for many years, and has been proved helpful in understanding the complex HiPIMS plasma discharge.<sup>30-32</sup> Raadu *et al.* built a global model using external discharge parameters such as geometry, pressure, and pulse waveforms as input.<sup>31</sup> It was able to describe the reactions in a simplified ionization region, determine the evolution of various species, and predict the ionization of metals. These models are usually quite complicated and time-consuming to setup. In many practical situations where diagnostics are costly to implement, it is

desirable to have a compact model to quickly estimate key parameters such as the ratio of the metal ion density to the gas ion density and allow an assessment of the self-sputtering effect. In this paper, such an attempt was made as to develop a semiempirical model based on some previous models. Some of predicted parameters were compared with the result from through-target flux measurements.

## II. EXPERIMENTAL SETUP

Experiments were performed in a large planar magnetron system with a 36 cm diameter Cu target. A Huettinger TruPlasma Highpulse 4002 DC Generator was used for HiPIMS. Pulsing parameters such as the charging voltage of the capacitor bank  $V_{ch}$ , pulse on-time  $t_p$ , and repetition frequency  $f$  could be varied. A typical set of discharge parameters was 800 V, 50  $\mu$ s, 100 Hz as the  $V_{ch}$ ,  $t_p$ , and  $f$ , while pressure was normally kept at 0.67 Pa. Details of the system were described elsewhere.<sup>16,17</sup> The magnetron uses a magnet pack behind the target to form a magnetic field for plasma confinement.  $B_{\parallel}$ , the magnetic flux intensity parallel to the target, was mapped right above the target surface, as shown in Fig. 1. The horseshoe-shaped field was designed for better deposition uniformity when rotating, which is a commonly used approach. Without rotation, the field will create an erosion racetrack with the same pattern.

In order to measure the species incident onto the target, a small orifice was drilled in the target, allowing the fluxes to penetrate and be measured on the other side. A special configuration was designed by modifying the magnetron, as illustrated in Fig. 2. The orifice was 2.5 mm. Originally 1 mm was used but later was increased to achieve a larger plasma flux and thus better signal-to-noise ratio. The orifice size was chosen with several considerations. First of all, it does not induce hollow cathode discharge to light up the hole nor lead to plasma instability for all the recipes tested. Second, it should not alter the plasma generation while having minimum perturbation to the ion extraction. For this to be satisfied, the orifice size should be ideally smaller than twice the sheath. High voltage Child formula has been used

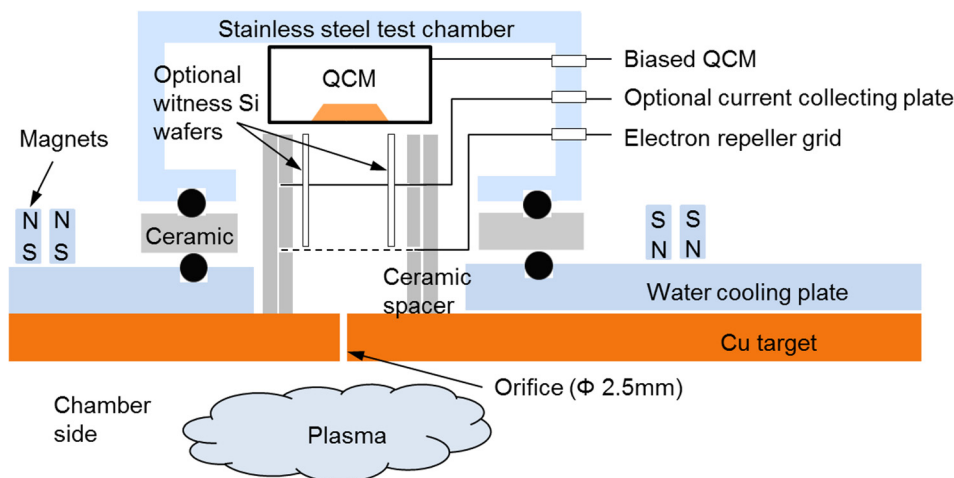


FIG. 2. (Color online) Schematic diagram of the assembly for through-target flux measurement.

to estimate the high voltage sheath in HiPIMS plasma to be  $\sim 1$  mm,<sup>33</sup> although it is not directly applicable due to the presence of a magnetic field and non-Maxwellian electrons. In the present study, the used average power densities were lower than the typical HiPIMS, and also the orifice was located in a region of weaker B field, so that relatively lower plasma densities are expected<sup>17</sup> as well as larger Debye length and sheath width. The requirement of small enough orifice size is thus expected to be met for most of time during the pulse, if not for the entire pulse, considering the plasma density increases about linearly during the period. Another factor to consider is the quite wide magnetic presheath with dramatic plasma potential drop in HiPIMS.<sup>33</sup> According to the study by Anders *et al.*,<sup>27,28</sup> the strong ionizations happen several millimeters away from the target in the presheath, as indicated by side-on images of the magnetron plasma. The perturbation to the ionization should then be minimal in this study. The plasma potential drop in the presheath will accelerate the ions before they even enter the sheath so any bending of ion trajectories entering the orifice will be reduced.

Vacuum of the system was maintained by enclosing the orifice with a small test chamber with o-ring sealing against the back of the target. The stainless steel test chamber was insulated from the target with a ceramic disk. The orifice was located within the racetrack groove with a local  $B_{||}$  of about 300 G, as shown in Fig. 1. The choice of the orifice location was limited by the geometry of the magnet pack.

Inside the test chamber, the ion current fluxes and the deposition fluxes were measured separately. For the ion current measurement, one layer of mesh placed about 8 mm behind the orifice was biased to as low as  $-600$  V to repel the electrons (as the electron repeller grid). A copper plate was placed approximately 10 mm behind the mesh with a typical bias of  $-500$  V to collect the current from Ar ions and Cu ions penetrating the mesh. The grid and the plate were placed inside a cylindrical ceramic housing and isolated from the test chamber. With varied bias on the plate, the ion energy distribution function could also be measured. In the deposition measurement configuration, the ion collection plate was removed. A QCM was placed 25 mm after the mesh to measure the deposition flux composed of Cu atoms and ions onto the QCM sensor. With the QCM isolated from electrical ground and biased between  $-600$  and  $+100$  V, the ions could either be admitted or repelled. In this way, the Cu atoms and ions could be distinguished. A similar concept has been used to measure the downstream metal ionization fractions (IFs).<sup>34</sup> There was concern that the pressure inside the test chamber could be relatively high with no differential pumping, causing scattering of the atoms and ions. Si wafers were then placed after the electron repeller grid, along the sidewall of the ceramic housing, to determine the scattered fluxes. The deposition thicknesses of Cu film on Si wafers were measured using cross-section scanning electron microscope (SEM). It should be mentioned that with electrons being screened by the electron repeller grid, no secondary discharge occurred in the test chamber within the used range of biases on current collecting plate and on QCM, which

would otherwise cause observable changes in collected current and in QCM signal.

### III. RESULTS AND DISCUSSION

#### A. Ion current measurement

The plasma currents were first measured on the electron repeller grid. They were composed of  $\text{Ar}^+$ ,  $\text{Cu}^+$ , and electrons. The collected currents at different biases on the electron repeller grid from  $-50$  to  $-600$  V are shown in Fig. 3(a). A recipe of 900 V, 50  $\mu\text{s}$ , 100 Hz, and 0.67 Pa was used here. At  $-50$  V, the current still consisted of many electrons, producing an overall negative current during the pulse. As the bias decreased, the collected current became more positive. It eventually saturated at about  $-500$  V, indicating all electrons were repelled and only ions were collected.

The ion current measured on the electron repeller grid ( $-500$  V) using different charging voltages of 750, 800, and 900 V are shown in Fig. 3(b). Comparison shows that the ion current increased with higher charging voltage. This is expected since the 900 V recipe produced a denser plasma. Consequently larger ion fluxes were generated flowing toward the target.

It is also noticed that the ion currents increased abruptly after a certain delay after the pulse started. On the contrary, the discharge currents on the target always increased smoothly (Fig. 4). The time delay to observe ion current

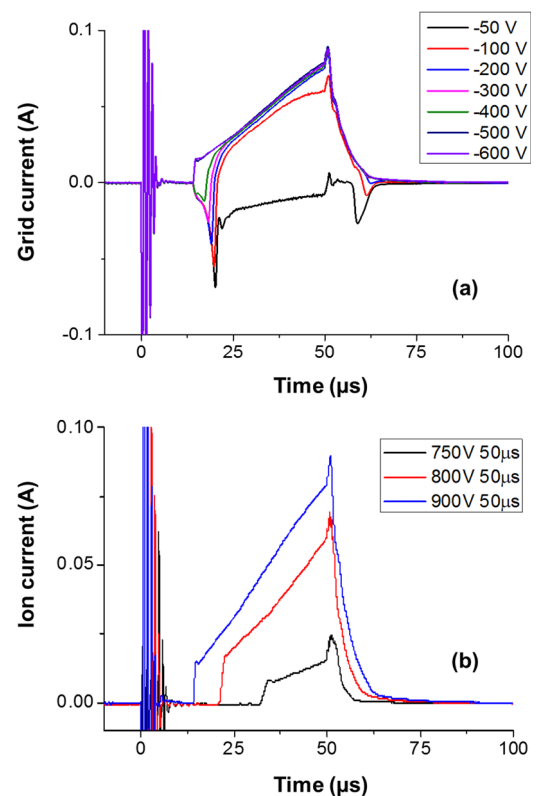


FIG. 3. (Color online) (a) Currents measured on the electron repeller grid at different biases on this grid using the recipe of 900 V, 50  $\mu\text{s}$ , 100 Hz, and 0.67 Pa. (b) Ion currents measured on the electron repeller grid ( $-500$  V) using different charging voltage of 750, 800, and 900 V. Other parameters were 50  $\mu\text{s}$ , 100 Hz, and 0.67 Pa.



depends on recipes. It is about  $31\text{ }\mu\text{s}$  for the 750 V recipe,  $21\text{ }\mu\text{s}$  for the 800 V recipe, and  $14\text{ }\mu\text{s}$  for the 900 V recipe. This abnormal observation may suggest a mechanism that plasmas are not directly ignited above the orifice. Instead, they are established in regions of stronger B field and drift along the racetrack to reach the orifice. Until then, no substantial plasma is present near the orifice. The plasma ignition being started in the stronger B field region is easy to understand. Electrons are better confined therein to build up higher electron density and thus facilitate the ionization process.

Two factors likely contribute to the shorter delay time for plasma to reach the orifice in higher voltage recipes. First, the drifting speed of electrons along the racetrack is higher with higher electric field as in the classical  $\mathbf{E} \times \mathbf{B}$  drift. It should be mentioned that recent studies from Anders *et al.*<sup>27,28</sup> showed that discrete hot ionization zones were formed with a current density higher than  $5.2\text{ A/cm}^2$ . And these localized zones drift at a speed lower than the typical  $\mathbf{E} \times \mathbf{B}$  drift. In present study the magnetron was operated at a lower current density than the threshold of localization of ionization, but continuing study will be performed with increased discharge current density to directly characterize the formation and drifting of the hot ionization zones. Second, with higher discharge voltage, plasma ignites in a longer strip along the racetrack extending further into the weaker B field region.

After the ion current is detected, it continues to increase. Figure 4(a) shows that within the  $50\text{ }\mu\text{s}$  pulses, it basically

tracks with the discharge current. However, in the  $100\text{ }\mu\text{s}$  pulses [Fig. 4(b)], the ion current can be seen to deviate from the discharge current with a shallower slope after approximately  $t = 65\text{ }\mu\text{s}$ . One hypothesis is that the deviation occurs when the entire ignition plasma stripe has passed the orifice. The drifting plasma still bears a resemblance to the initial shape of the ignition plasma. Of course, the plasma continues to grow more intense over the entire racetrack so that the ion current does not drop to zero after  $t = 65\text{ }\mu\text{s}$ .

## B. Differentiation of ion species

The ion fluxes measured above included both  $\text{Ar}^+$  and  $\text{Cu}^+$  ions. It is desirable to distinguish these two species. The deposition fluxes of  $\text{Cu}^+$  and Cu atoms were measured on the QCM sensor and on the witness Si wafers as described in Sec. II, while ion currents including  $\text{Ar}^+$  and  $\text{Cu}^+$  were measured on the electron repeller grid. The electron repeller grid was biased at  $-500\text{ V}$  to attract ions, and  $-50\text{ V}$  to reduced ions. In the DC magnetron plasma where most voltage drops within the thin sheath, ions generated in the bulk plasma region will be accelerated toward the target to have energies of about the full sheath voltage. In HPPMS discharge, the sheath usually does not fully collapse within short pulses, and ions can be generated in a wide presheath in front of the target.<sup>17,35</sup> The plasma potential varies with the distance to the target, so that ions are accelerated into the orifice with different energies. Also, ions may impinge on the side wall of the orifice to further lose energy. Changing the grid bias ( $V_g$ ) from  $-500$  to  $-50\text{ V}$  could thus greatly reduce the penetrating ions, though not able to repel ions completely. More positive bias on the grid had been attempted but unfortunately led to unstable secondary plasma. The QCM was kept at  $-500\text{ V}$ .

The recipe of 900 V,  $50\text{ }\mu\text{s}$ , 100 Hz, and 0.67 Pa was run for a total time of 70 min to deposit thick enough films on the wafer. Thicknesses at different points on the wafer were determined with cross-section SEM. Figure 5 shows the film thicknesses as a function of the distance from the electron repeller grid. At either bias, the deposition thickness kept decreasing as distance from the grid increased, clearly showing the effect of scattering. By changing the bias ( $V_g$ ) from  $-500\text{ V}$  to  $-50\text{ V}$ , more ions were repelled by the grid, resulting in lower film thicknesses. The deposition profile from the Cu ions can be calculated as the subtraction of the two curves, also shown in Fig. 5. The remaining deposition at  $V_g = -50\text{ V}$  was from Cu atoms and some high energy Cu ions which were not repelled by the grid bias.

To further understand the deposition profiles on the witness wafers and estimate the fluxes of various species, a simplified model on gas scattering inside the test chamber is developed.<sup>36</sup> This is a Monte-Carlo simulation to follow the path traversed by an initialized test atom or ion as it is introduced into a gaseous chamber environment with a preset energy, direction, and location, and sent along the axial direction (from the orifice toward the QCM). For the currently work, the exact ion energy distribution function is unknown and such measurements are not within the scope of

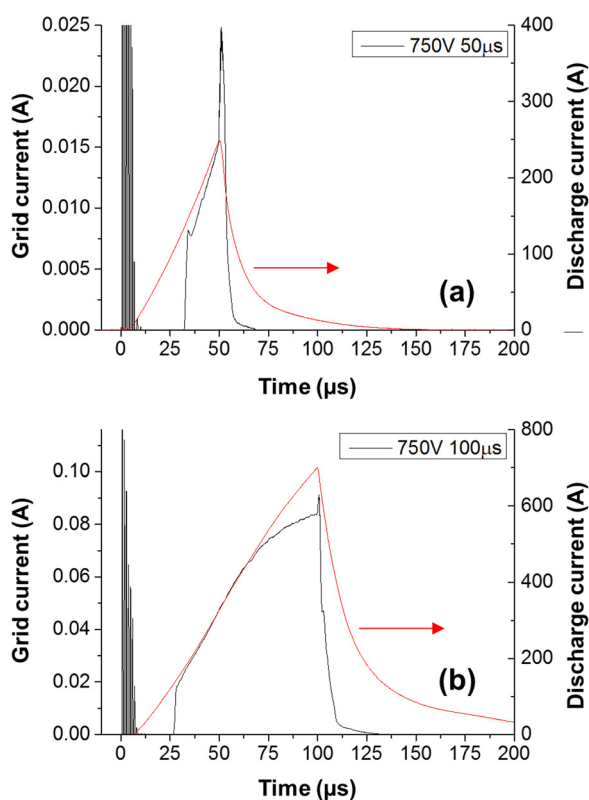


FIG. 4. (Color online) Ion current measured on the grid as compared with the discharge current in (a)  $50\text{ }\mu\text{s}$  and (b)  $100\text{ }\mu\text{s}$  pulses:  $V_{\text{ch}} 750\text{ V}$  and  $0.67\text{ Pa}$ .

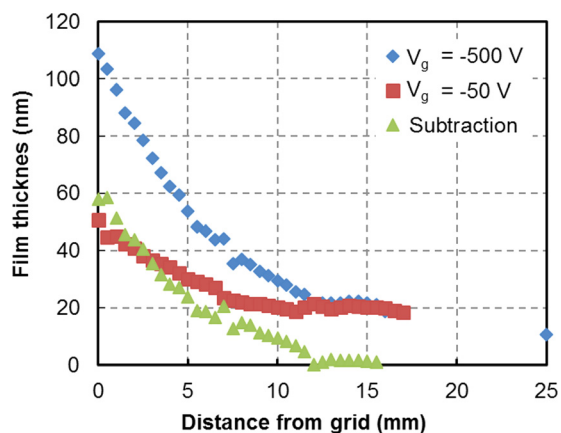


FIG. 5. (Color online) Deposition thicknesses on the Si witness wafer as a function of the distance to the electron repeller grid. The point at 25 mm was from QCM measurement. Two different grid biases  $V_g$  of  $-500$  and  $-50$  V were used. At  $-50$  V, the deposition flux is comprised of atoms and high energy ions. The subtraction of the two is the signal of low energy ions and is also shown.

study. To allow further analysis, a reasonable simplification was made to divide the ions into two groups, fast ions with a single energy of  $400$  eV after the hole and slower ions of  $200$  eV after the hole. Here,  $400$  eV is about the stabilized voltage on the target for currently used recipe, while  $200$  eV ions account for the ones which are generated in the pre-sheath where the plasma potential is more negative relative to the bulk plasma and which may endure certain energy loss through collisions. The density ratio of the two groups will be calculated to best match the experimental deposition profile. The initial location of these species is modeled as uniformly distributed on the surface of the orifice. The neutrals are modeled using the same distribution but with an initial energy of  $3$  eV as commonly used for the sputtered atoms. The geometries can be seen in Fig. 6.

As each species travels through the test chamber, the model tests whether a gas collision has occurred. The gas collision cross section is derived using interatomic potentials calculated by an Abrahamson potential coupled with an attractive well.<sup>37,38</sup> If a collision is deemed to have occurred in a given step length, the collision is then carried out using classical scattering theory. An impact parameter is chosen as  $b = b_{\max} a^{0.5}$ , where  $b_{\max}$  is the value at which scattering is less than  $1^\circ$ , and  $a$  is a random number between  $0$  and  $1$ . Once the test atom/ion has deposited, or reached threshold energy of  $0.001$  eV, the code is stopped and repeated for the next test atom. In total,  $1000$  test atoms were used for each measurement.

As discussed previously, Cu atoms and fast ions can penetrate the grid at a bias of  $-50$  V. The simulation results of the Cu atom deposition and the fast ion deposition at  $13.3$  Pa are shown in Fig. 6(a), as compared with the measured thicknesses on the witness wafers. It can be seen that the neutral deposition on the sidewall quickly decreases farther away from the grid. The simulated deposition profile of fast ions, however, reaches a maximum at about  $10$  mm away from the grid and remains high for a long range. It also allows some

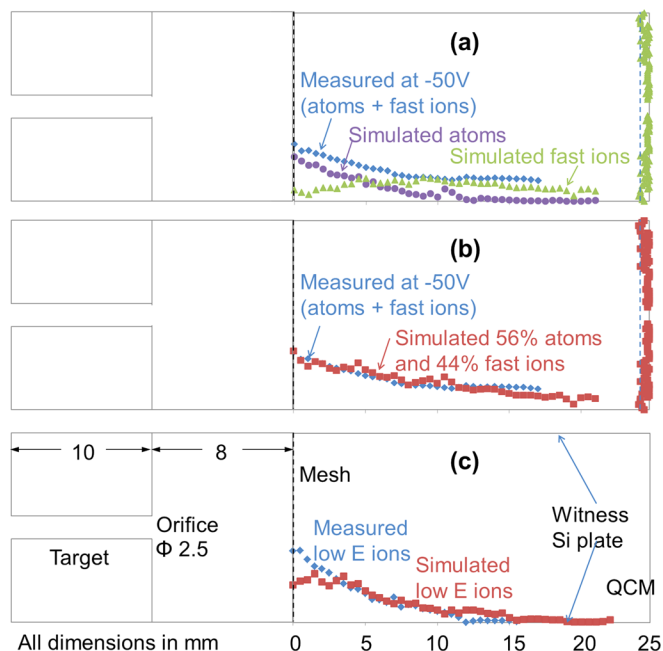


FIG. 6. (Color online) (a) Deposition profiles by neutral atoms and fast ions on the side wall and bottom wall based on the simulation at  $13.3$  Pa. Also shown is the measured deposition thickness on the Si witness wafer along the sidewall at  $-50$  V grid bias. The dashed line shows the equivalent thickness measured on the QCM. (b) The measured deposition profile is fitted with the simulated data with  $56\%$  atoms and  $44\%$  fast ions in the flux. (c) The simulated deposition profile on the side wall by  $200$  eV ions based on the simulation at  $13.3$  Pa, as compared with the measured results for low energy ions (the subtraction curve in Fig. 5).

deposition on the QCM. Such a deposition profile by the fast ions helps explain the seemingly saturated thickness measured after  $12$  mm. The calculated deposition thicknesses by these two species are added up with different trial ratios of their concentrations. And with  $56\%$  atoms and  $44\%$  fast ions, the simulation results best fit the experimental results, as illustrated in Fig. 6(b).

Ions of lower energies than the target potential also exist. The simulation results of ions with lower energy ( $200$  eV) at  $13.3$  Pa are given in Fig. 6(c). It can be seen that the simulated deposition on the sidewall decreases from the grid toward the QCM. This agrees with the measured deposition profile by low energy ions found from the subtraction in Fig. 5.

Going back to Fig. 5, the deposition thicknesses are integrated over the entire witness wafer to get the total deposition fluxes at  $-500$  and  $-50$  V, respectively. The fluxes of  $\text{Cu}^0$  atoms and  $\text{Cu}^+$  ions are then calculated based on the ratios from the simulation. It is determined that there are about  $40\%$  of  $\text{Cu}^+$  ions in total Cu flux. Comparing the total  $\text{Cu}^+$  ions flux with the ion current collected on grid (including both  $\text{Cu}^+$  and  $\text{Ar}^+$ ), the ratio of  $\text{Cu}^+$  to  $\text{Ar}^+$  is then determined to be about  $1.5 \pm 0.3$ . It should be reminded that this estimation is based on a reasonably simplified ion energy distribution.

The results indicate a substantial fraction of ions incident onto the target are  $\text{Cu}^+$  ions. The importance of self-sputtering of Cu in HiPIMS is thus directly confirmed by the

through-target flux measurements. With a higher power density, this fraction is expected to further increase.

#### IV. SEMIEMPIRICAL IONIZATION MODEL

##### A. Model description

The through-target flux measurements were able to achieve the important parameter of  $\text{Cu}^+$  to  $\text{Ar}^+$  ratio in HiPIMS plasma. However, it would be much more convenient to quickly predict the ratio without complicated experimentation. For this purpose, a time-dependent model is developed to describe the ionization reactions inside the high-powered pulsed-plasma. By using some experimental data such as the pulse voltage and current, the semiempirical model is able to predict the instantaneous densities of different species, including electrons, metal atoms, and ions of both metal and argon.

The model is built to describe the ionization zone in vicinity of the target. Some previous modeling work by a number of research groups has been studied and used as good references.<sup>30,31</sup> In a pulsed magnetron, the magnetic field defines a region with effective plasma confinement. Ionizations are greatly enhanced in this region of intense plasma, leading to the erosion racetrack formation. The geometry of the ionization zone is shown in a schematic diagram (Fig. 7). For simplicity, it is assumed to have a lateral size the same as the racetrack width  $w$ , and in the axial direction, it is between  $z_1$  and  $z_2$ . Here,  $z_1$  is the sheath width, while  $z_2$  is determined by the magnetic field topology. Typically the  $z_1$  value is quite small (e.g., 1 or 2 mm), while  $z_2$  is between 1 and 3 cm, according to the literature.<sup>31</sup>

The species considered in the model are the electrons, metal atoms  $M^0$  and ions  $M^+$ , Ar atoms  $\text{Ar}^0$  and  $\text{Ar}^+$  ions. Specifically, the metal studied here is Cu. Electrons are emitted from the target and gain energy from the sheath. They lose the energy through excitations and ionizations. The reaction rates depend on the electron energies in the plasma. The generated ions are then accelerated toward the target and induce sputtering in the racetrack. The ejected metal atoms will traverse through the plasma and get partially ionized. The degree of ionization again depends on the instantaneous plasma properties.

Figure 8 shows a block diagram illustrating the structure of the model. The input parameters are in the ovals and the calculated parameters are in the rectangles. Among the input parameters there are: discharge voltage  $U_d(t)$ , current  $I_d(t)$ ,

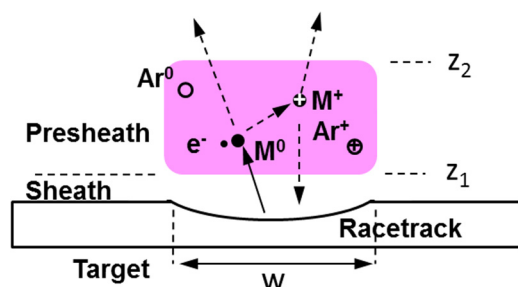


FIG. 7. (Color Online) Schematic diagram showing the ionization region.

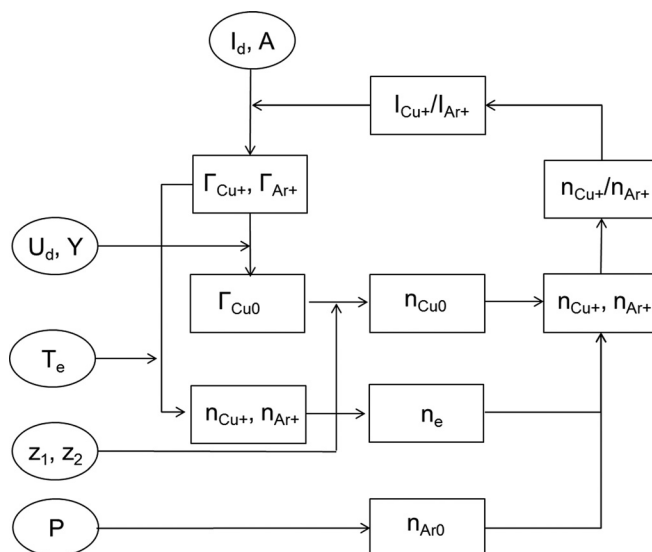


FIG. 8. Block diagram showing the structure of the model.

and pressure  $P$ , which can be easily measured.  $U_d$  determines the sheath voltage and thus the incident ion energies. The sputtering yields of Cu by  $\text{Cu}^+$  and  $\text{Ar}^+$  are calculated accordingly. The discharge voltage also affects the secondary electron emission (SEE) and their energies after sheath acceleration. Technically, by just using  $U_d(t)$  as the input, one should be able to predict the entire HiPIMS discharge including the discharge current. However, by using current  $I_d(t)$  as an input, the model can be greatly simplified and more accurate. For example, the secondary electron emission process can be left out of the model.  $I_d(t)$  includes both the  $\text{Ar}^+$  and  $\text{Cu}^+$  components, whose relative ratio varies over time and is calculated in the model. Other input parameters include the dimensions of the ionization region. The racetrack width  $w$  is measured and used as the width of the ionization zone. One millimeter is used for the sheath width  $z_1$ . The height  $z_2$  is chosen to be 1.5 cm for initial tests based on the fact that the measured parallel B field at 1.5 cm above the racetrack reduces to about a half of that at the target surface. Different numbers for  $z_1$  and  $z_2$  were tried, and it was shown that the modeling results were not very sensitive on their values. Uniform  $n_e$  and  $T_e$  are assumed in this region. The Cu atom density varies along the axial direction considering several microseconds are needed for Cu atom flux to pass the ionization zone. An average Cu atom density from integration over the entire region is used for the Cu atom ionization process.  $T_e$  is another input parameter which can be predicted based on triple Langmuir probe measurements.<sup>16</sup> This eliminates the need for including all of the loss mechanisms in the power balance equation.

In the model, densities of different species including  $n_e$ ,  $n_{\text{Cu}}^0$ ,  $n_{\text{Ar}}^0$ ,  $n_{\text{Cu}}^+$ , and  $n_{\text{Ar}}^+$  are calculated for each time step of 0.1  $\mu\text{s}$ . With increased  $n_e$  (from increased  $I_d$ ) and  $n_{\text{Cu}}^0$  (from more intense sputtering),  $n_{\text{Cu}}^+$  and  $n_{\text{Ar}}^+$  are recalculated at the end of each time step. The ratio of  $n_{\text{Cu}}^+$  to  $n_{\text{Ar}}^+$ , combined with the instantaneous current, is used to determine the new  $n_{\text{Cu}}^+$  and  $n_{\text{Ar}}^+$  for the next step. The details of the calculations are described below.

- (1) Prediction of  $n_{\text{Cu}^+}$ ,  $n_{\text{Ar}^+}$ , and  $n_e$ : The discharge current  $I_d$  is composed of Ar ion current  $I_{\text{Ar}^+}$  and Cu ion current  $I_{\text{Cu}^+}$  and the secondary electron emission current induced by these ions

$$I_d = I_{\text{Ar}^+}(1 + \gamma_{\text{Ar}^+}) + I_{\text{Cu}^+}(1 + \gamma_{\text{Cu}^+}). \quad (1)$$

The SEE coefficient induced by  $\text{Ar}^+$  on Cu target,  $\gamma_{\text{Ar}^+}$ , is about 0.1 (Ref. 39) and the same value of  $\gamma_{\text{Cu}^+}$  is used for  $\text{Cu}^+$  on Cu target. At the beginning, there is only  $\text{Ar}^0$  in the chamber, so the plasma contains only electrons and  $\text{Ar}^+$ . The density of  $\text{Ar}^+$ ,  $n_{\text{Ar}^+}$ , can then be determined

$$I_{\text{Ar}^+} = n_{\text{Ar}^+} e u_B (\text{Ar}^+) A. \quad (2)$$

This is based on the mechanism that ions are accelerated to Bohm velocity at the sheath-presheath edge and the flux remains the same in the sheath.<sup>40</sup> Similar calculations can be done for  $\text{Cu}^+$

$$I_{\text{Cu}^+} = n_{\text{Cu}^+} e u_B (\text{Cu}^+) A. \quad (3)$$

The Bohm velocity depends on the electron temperature  $T_e$  and the mass of either  $\text{Cu}^+$  or  $\text{Ar}^+$  ions

$$u_B = \left( \frac{e T_e}{M} \right)^{\frac{1}{2}}. \quad (4)$$

Other parameters in these equations include  $e$  as the elementary charge,  $A$  as the racetrack area, and  $M$  as the mass of ions. Electron density is just calculated as the sum of  $n_{\text{Cu}^+}$  and  $n_{\text{Ar}^+}$ , based on the charge neutrality in the plasma

$$n_e = n_{\text{Ar}^+} + n_{\text{Cu}^+}. \quad (5)$$

Prediction of  $n_{\text{Cu}^0}$  from sputtering: The Cu target is sputtered by both  $\text{Ar}^+$  and  $\text{Cu}^+$  ions with their own sputtering yields. The total flux of Cu atoms  $\Gamma_{\text{Cu}^0}$  is calculated with  $\Gamma_{\text{Ar}^+}$  and  $\Gamma_{\text{Cu}^+}$  obtained from the step (1) with the known racetrack area  $A$ .

$$\Gamma_{\text{Cu}^0} = \Gamma_{\text{Ar}^+} Y_{\text{Ar}^+} + \Gamma_{\text{Cu}^+} Y_{\text{Cu}^+}. \quad (6)$$

These Cu atoms have an average energy between 1 and 3 eV leaving the target,<sup>40</sup> which can then be used to calculate an average speed  $v_0$ . At 2 eV, the Cu atoms have a speed of about  $1.7 \times 10^3$  m/s. The density of Cu atoms  $n_{\text{Cu}^0}$  can then be determined using Eq. (7). It should be noted that at this speed, Cu atoms need about 8.6  $\mu\text{s}$  to penetrate the ionization zone of 1.5 cm. As a result, the Cu atom density in the region is not uniform even when no scattering collisions take place. An average Cu atom density in the region is calculated for each time step

$$\Gamma_{\text{Cu}^0} = n_{\text{Cu}^0} v_0. \quad (7)$$

- (2) Rarefaction effect: During HiPIMS, the fast sputtered metal atoms will have collisions with the background Ar atoms. This “sputtering wind” thus reduces the argon

density. An accurate prediction of the argon density loss requires the knowledge of the densities of different species including  $\text{Cu}^0$  and  $\text{Cu}^+$  as well as their velocity distributions, based on which detailed calculations of the momentum transfer can be made. Instead, a simplified method is used in order to include this effect in the model. The argon density is reduced to keep the pressure in the region constant.

- (3) Ionization processes: The ionization rate is described below. It is proportional to both the neutral and electron densities. Here,  $K_{iz}$  is the ionization rate coefficient based on the ionization cross sections and the electron energy distributions.

$$\frac{dn_{\text{Cu}^+}}{dt} = n_0 n_e K_{iz}, \quad (8)$$

$$K_{iz} = \langle \sigma_{iz} v_e \rangle. \quad (9)$$

The electron impact ionization and Penning ionization are considered with the cross-sections taken from literatures.<sup>31,41</sup> The energy distribution is assumed to be Maxwellian for the calculation of  $K_{iz}$ . The ion loss is also accounted for by subtracting the target-directed ion flux, as shown in Eq. (10), which uses  $V$  as the racetrack volume. A new  $n_{\text{Cu}^+}$  is calculated for each short time step. Similar calculation is done for Ar ions.

$$V \frac{dn_{\text{Cu}^+}}{dt} = V n_0 n_e K_{iz} - n_{\text{Cu}^+} e u_B (\text{Cu}^+) A. \quad (10)$$

- (4) Time development: With a newly calculated  $n_{\text{Cu}^+}$  and  $n_{\text{Ar}^+}$ , in principle, the model can determine the total current and continue. To avoid inconsistency with the input  $I_d(t)$  data, only the ratio of the  $n_{\text{Cu}^+}$  and  $n_{\text{Ar}^+}$  is kept for the next time step. New  $I_{\text{Ar}^+}$  and  $I_{\text{Cu}^+}$  are determined based on this ratio and  $I_d(t)$  to continue the calculation.

## B. Modeling results

The discharge condition used in the through-target flux measurement is subjected to the model calculation.  $V_{\text{ch}}$ ,  $t_p$ , and  $f$  were 900 V, 50  $\mu\text{s}$ , 100 Hz individually, and the pressure was 0.67 Pa. The racetrack area was measured to be 422.8  $\text{cm}^2$ .

The model results are shown in Fig. 9. Electron density  $n_e$  is seen to have a similar trend as the discharge current  $I_d$  and increase up to  $5.8 \times 10^{19} \text{ m}^{-3}$ . The  $\text{Ar}^+$  ions are the main ion species at the beginning with an increasing  $n_{\text{Ar}^+}$ . It decreases later due to the gas rarefaction effect, i.e., fewer Ar atoms to be ionized. The  $\text{Cu}^+$  density  $n_{\text{Cu}^+}$  increases more rapidly and becomes dominant after 30  $\mu\text{s}$ . This is because of an increasing Cu neutral density (not shown here). The Cu IF increases to 32% and the Ar IF increases to 20%. Such values are lower than what are typically reported for the HiPIMS discharge. This is likely caused by the lower average current density in this experiment with regards to the literature (about 1.7 A/ $\text{cm}^2$  on average, as compared to 5.2 A/ $\text{cm}^2$  in Ref. 27 when strong plasma localization occurred). Due to the large size of the target, it is difficult to



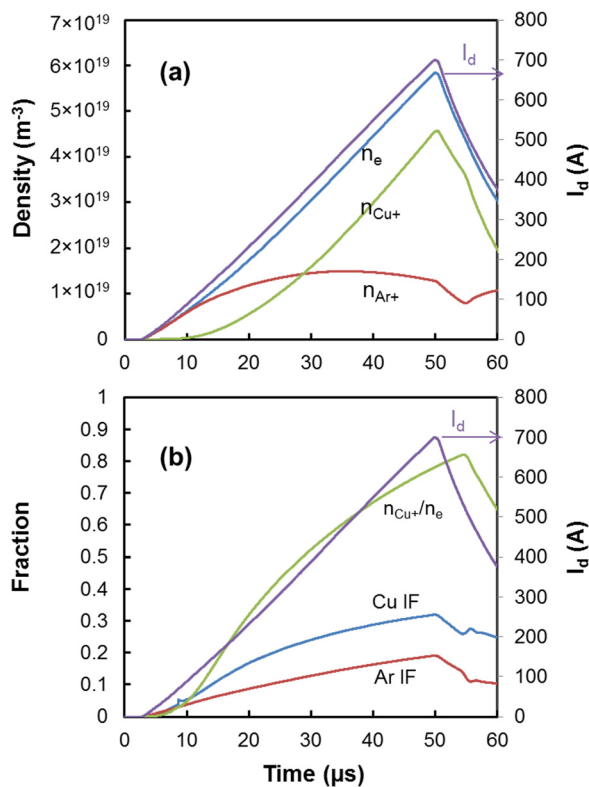


FIG. 9. (Color online) Model results for the recipe of 900 V, 50  $\mu\text{s}$ , 100 Hz, and 0.67 Pa. (a) The electron density and the densities of  $\text{Ar}^+$  and  $\text{Cu}^+$ . (b) The ionization fractions of Cu and Ar, and the fraction of  $\text{Cu}^+$  in total ions ( $n_{\text{Cu}^+}/n_e$ ). In both figures, the input discharge current is shown for time reference.

apply a  $V_{\text{ch}}$  of 1000 V or higher while maintaining a stable discharge. This leads to a relatively low  $n_e$  for ionization enhancement.

The fraction of  $\text{Cu}^+$  ions in total ions reaches 82% before the pulse ends. This shows that the system is almost completely self-sputtering at the end of the pulse. In the through-target diagnosis, a density ratio of  $\text{Cu}^+$  to  $\text{Ar}^+$  was measured as  $1.5 \pm 0.3$ . This is an average value over the entire pulse duration. For comparison, the time-averaged value of  $n_{\text{Cu}^+}/n_{\text{Ar}^+}$  ratio from  $t = 0$  to  $t = 50 \mu\text{s}$  from the model is 1.4. Such a prediction matches with the experimental result very well, and both show an enhanced self-sputtering in the HiPIMS discharge. In all, the model is shown to be useful to quickly predict some key parameters in HiPIMS and to quantify the critical processes such as the self-sputtering. Appropriate assumptions are able to simplify the model while highlighting the key mechanisms.

## V. SUMMARY

The self-sputtering effect in the HPPMS system was characterized by directly measuring the recirculating ion fluxes through a sampling orifice located in racetrack region on a Cu target.  $\text{Ar}^+$  ions,  $\text{Cu}^+$  ions, and Cu atoms were deconvoluted by using diagnostics including grids with varied biases to collect ion currents and witness Si wafers to measure the deposition flux. The sampled ion currents were observed to increase abruptly after a certain delay into the pulse. It is

believed plasmas were ignited initially in a stripe of stronger B field and drifted along the racetrack to reach the orifice. Under a higher pulse voltage, plasma ignition region became longer and drifted faster toward the region of weak magnetic field.

The recirculating ions were shown to have different energies, likely due to varied plasma potentials in a wide pre-sheath where ions are generated. With the gas scattering in the test chamber taken into consideration, the ratio of  $\text{Cu}^+$  density to  $\text{Ar}^+$  density was determined to be  $1.5 \pm 0.3$ , indicating an enhanced self-sputtering during HPPMS.

A compact plasma model has been developed to depict the ionization process in the intense plasma region and to quickly predict some key parameters in HPMS. Experimental data such as the discharge voltage and current waveforms were used as input. The time-dependent densities of electrons, ions, and atoms were determined. Under the same condition for through-target flux measurement, the ratio of  $\text{Cu}^+$  density to  $\text{Ar}^+$  density was estimated to be 1.4, matching the experimental result. The model can be beneficial for practical use when diagnostics are costly and time-consuming to implement.

## ACKNOWLEDGMENTS

This study was supported by the Center for Lasers and Plasma in Advanced Manufacturing (National Science Foundation, Grant No. CMMI09-53057). The authors would like to acknowledge Huettinger Electronic for providing the pulsed plasma generator and MechSE Machine Shop for modifying the magnetron system. The SEM characterization was carried out in part in the Frederick Seitz Materials Research Laboratory Central Facilities, University of Illinois.

- <sup>1</sup>S. M. Rossnagel, *Semicond. Int.* **21**, 99 (1996).
- <sup>2</sup>J. A. Hopwood, *Ionized Physical Vapor Deposition*, Thin Film Series Vol. 27, edited by J. A. Hopwood (Academic, San Diego, 2000).
- <sup>3</sup>D. V. Mozgrin, I. K. Fetisov, and G. V. Khodachenko, *Plasma Phys. Rep.* **21**, 400 (1995).
- <sup>4</sup>V. Kouznetsov, K. Macák, J. M. Schneider, U. Helmersson, and I. Petrov, *Surf. Coat. Technol.* **122**, 290 (1999).
- <sup>5</sup>J. T. Gudmundsson, N. Brenning, D. Lundin, and U. Helmersson, *J. Vac. Sci. Technol. A* **30**, 030801 (2012).
- <sup>6</sup>J. Lin, J. J. Moore, W. D. Sproul, B. Mishra, J. A. Rees, Z. Wu, R. Chistyakov, and B. Abraham, *Surf. Coat. Technol.* **203**, 3676 (2009).
- <sup>7</sup>L. Meng, A. N. Cloud, S. Jung, and D. N. Ruzic, *J. Vac. Sci. Technol. A* **29**, 011024 (2011).
- <sup>8</sup>K. Sarakinos, J. Alami, and S. Konstantinidis, *Surf. Coat. Technol.* **204**, 1661 (2010).
- <sup>9</sup>J. Alami, S. Bolz, and K. Sarakinos, *J. Alloys Compd.* **483**, 530 (2009).
- <sup>10</sup>A. P. Eghasarian, J. G. Wen, and I. Petrov, *J. Appl. Phys.* **101**, 054301 (2007).
- <sup>11</sup>J. Alami, P. O. Å. Persson, J. Böhlmark, J. T. Gudmundsson, D. Music, and U. Helmersson, *J. Vac. Sci. Technol. A* **23**, 278 (2005).
- <sup>12</sup>J. W. Bradley, H. Bäcker, P. J. Kelly, and R. D. Arnell, *Surf. Coat. Technol.* **135**, 221 (2001).
- <sup>13</sup>J. Alami, J. T. Gudmundsson, J. Böhlmark, J. Birch, and U. Helmersson, *Plasma Sources Sci. Technol.* **14**, 525 (2005).
- <sup>14</sup>Th. Welzel, Th. Dunger, H. Kupfer, and F. Richter, *J. Appl. Phys.* **96**, 6994 (2004).
- <sup>15</sup>P. M. Bryant, S. A. Voronin, J. W. Bradley, and A. Vetushka, *J. Appl. Phys.* **102**, 043302 (2007).
- <sup>16</sup>H. Yu, L. Meng, M. Szott, J. T. Meister, T. S. Cho, and D. N. Ruzic, *Plasma Sources Sci. Technol.* **22**, 045012 (2013).

- <sup>17</sup>L. Meng, H. Yu, M. M. Szott, J. T. McLain, and D. N. Ruzic, *J. Appl. Phys.* **115**, 223301 (2014).
- <sup>18</sup>A. P. Ehiasarian, R. New, W.-D. Münz, L. Hultman, U. Helmersson, and V. Kouznetsov, *Vacuum* **65**, 147 (2002).
- <sup>19</sup>S. Konstantinidis, J. P. Dauchot, M. Ganciu, A. Ricard, and M. Hecq, *J. Appl. Phys.* **99**, 013307 (2006).
- <sup>20</sup>J. Bohlmark, M. Lattemann, J. T. Gudmundsson, A. P. Ehiasarian, Y. A. Gonzalvo, N. Brenning, and U. Helmersson, *Thin Solid Films* **515**, 1522 (2006).
- <sup>21</sup>S. M. Rossnagel and H. R. Kaufman, *J. Vac. Sci. Technol. A* **6**, 223 (1988).
- <sup>22</sup>J. Alami, K. Sarakinos, G. Mark, and M. Wuttig, *Appl. Phys. Lett.* **89**, 154104 (2006).
- <sup>23</sup>C. Huo, M. A. Raadu, D. Lundin, J. T. Gudmundsson, A. Anders, and N. Brenning, *Plasma Sources Sci. Technol.* **21**, 045004 (2012).
- <sup>24</sup>A. Anders, J. Andersson, and A. P. Ehiasarian, *J. Appl. Phys.* **102**, 113303 (2007).
- <sup>25</sup>A. Anders, J. Capek, M. Hala, and L. Martinu, *J. Phys. D: Appl. Phys.* **45**, 012003 (2012).
- <sup>26</sup>A. Ehiasarian, A. Hecimovic, T. de los Arcos, R. New, V. Schulz-von der Gathen, M. Boke, and J. Winter, *Appl. Phys. Lett.* **100**, 114101 (2012).
- <sup>27</sup>A. Anders, *Appl. Phys. Lett.* **100**, 224104 (2012).
- <sup>28</sup>A. Anders, P. Ni, and A. Rauch, *J. Appl. Phys.* **111**, 053304 (2012).
- <sup>29</sup>A. V. Kozyrev, N. S. Sochugov, K. V. Oskomov, A. N. Zakharov, and A. N. Odivanova, *Plasma Phys. Rep.* **37**, 621 (2011).
- <sup>30</sup>D. J. Christie, *J. Vac. Sci. Technol. A* **23**, 330 (2005).
- <sup>31</sup>M. A. Raadu, I. Axnäs, J. T. Gudmundsson, C. Huo, and N. Brenning, *Plasma Sources Sci. Technol.* **20**, 065007 (2011).
- <sup>32</sup>N. Brenning, I. Axnäs, M. A. Raadu, D. Lundin, and U. Helmersson, *Plasma Sources Sci. Technol.* **17**, 045009 (2008).
- <sup>33</sup>A. Rauch, R. J. Mendelsberg, J. M. Sanders, and A. Anders, *J. Appl. Phys.* **111**, 083302 (2012).
- <sup>34</sup>L. Meng, R. Raju, R. Flauta, H. Shin, D. N. Ruzic, and D. B. Hayden, *J. Vac. Sci. Technol. A* **28**, 112 (2010).
- <sup>35</sup>A. Mishra, P. J. Kelly, and J. W. Bradley, *Plasma Sources Sci. Technol.* **19**, 045014 (2010).
- <sup>36</sup>J. Sporre, "Diagnosis of the flux emanating from the intermediate focus of an extreme ultraviolet light lithography source," Ph.D. thesis, University of Illinois at Urbana-Champaign, 2013.
- <sup>37</sup>A. A. Abrahamson, *Phys. Rev.* **178**, 76 (1969).
- <sup>38</sup>A. M. Myers, D. N. Ruzic, and J. R. Doyle, *J. Appl. Phys.* **72**, 3064 (1992).
- <sup>39</sup>A. V. Phelps and Z. Lj. Petrovic, *Plasma Sources Sci. Technol.* **8**, R21 (1999).
- <sup>40</sup>M. A. Lieberman and A. J. Lichtenberg, *Principles of Plasma Discharge and Materials Processing* (Wiley, New York, 1994).
- <sup>41</sup>R. S. Freund, R. C. Wetzel, R. J. Shul, and T. R. Hayes, *Phys. Rev. A* **41**, 3575 (1990).